

Article

Concrete–Concrete Bond in Mode-I: A study on the Synergistic Effect of Surface Roughness and Fiber Reinforcement

Bardia Kabiri Far and Cristina Zanotti * 

Civil Engineering Department, The University of British Columbia, 6250 Applied Science Lane, Vancouver, BC V6T 1Z4, Canada; bardia.kabirifar@gmail.com

* Correspondence: czanotti@civil.ubc.ca; Tel.: +1-604-822-4471

Received: 17 April 2019; Accepted: 18 June 2019; Published: 22 June 2019



Abstract: Effectiveness and durability of interventions on deficient concrete structures remain a major concern, comprising the challenge of old-to-new concrete compatibility and bonding, as stress concentrations and microstructural flaws at the old-to-new concrete interface compromise structural integrity and create migration paths for harmful contaminants. Fiber reinforcement can be beneficial, but proper quantification and mastering of fundamental mechanisms is required before these are fully utilized. A study is presented on Mode-I crack growth resistance at the interface between two concretes (substrate and repair). Countered Double Cantilever Beam tests are performed, crack growth resistance curves calculated (Modified Linear Elastic Fracture Mechanics), and complemented with analysis of interfacial roughness and failure planes. Polyvinyl alcohol (8 and 12 mm length) and steel fibers (13 mm) are introduced in the repairs at 0.5% and 1% volume fractions. Results indicate that fibers improve fracture behavior of both the repair material and substrate–repair interface; correlations with interfacial roughness, crack deviation, and fracture parameters are discussed.

Keywords: concrete–concrete bond; Mode-I; repair and retrofit; roughness quantification; fiber reinforced concrete

1. Introduction

In order to extend the service life of deteriorating reinforced concrete structures, and to grant safety in the case of increased loading demand, interventions of repair and rehabilitation have become of frequent practice worldwide. Nevertheless, poor compatibility and debonding of the repair material can jeopardize these interventions. In a repaired system, the interface between the concrete substrate and the new repair layer is typically weaker than the materials on either side. Due to such weakness, combined to stress concentrations (emphasized in case of poor substrate–repair compatibility), the interface is much more vulnerable to cracking and failure. As a result, the performance of repaired systems and, thus, their safety and durability, are highly dependent on the properties of the interface [1–5]. Fiber reinforced concrete (FRC) is recognized as a promising option for improving concrete durability [6–9]. These benefits become even more relevant in repaired structures, where fibers can help improve compatibility to the substrate or, at least, reduce the extent of damage arising from poor compatibility [8,10].

It has been proven that fiber reinforcement can also improve the bond of a repair concrete layer to an existing substrate, though this is highly dependent on several factors including substrate preparation and roughness, fiber bonding, size, aspect ratio, and stiffness, type of stress applied at the interface, etc. Lim and Li [11] investigated the bond strength, failure mode, and cracking behavior of Engineered Cementitious Composites (ECC) and introduced the concept of interface crack trapping. Their test results indicate that the ECC repair system has higher strength, more ductile behaviour, and better crack width control [12]. Wagner et al. [13] studied the interface between strain

hardening cementitious repair layers and concrete substrate. The researchers concluded that bond strength was highly affected by surface roughness and added the qualitative observation that the beneficial effect of fiber reinforcement was impacted by the amount of repair material that remained attached to the substrate after failure (in other words, by the deviation between failure and bond plane). Slowik et al. [14] characterized the behaviour of strain-hardening cement-based composite systems aimed at enhancing the overall durability of structural retrofits, by addressing both interfacial behaviour and drying shrinkage. Zanotti et al. [15,16] studied the interface behaviour under both tensile and shear loading. The results show the effectiveness of fibers in enhancing the quality of the interface both in tension and in shear. Further studies investigated the effect of fiber properties and surface preparation on the shear bond strength of substrate-repair interfaces in mixed modes of fracture. It was found that surface preparation has a strong effect on the crack deviation from the interface followed by fiber activation and multiple cracking before failure. A study by Banthia et al. [17] explored the suitability of fiber-reinforced cementitious composites with high-volume fractions of microfibers for thin repair applications. Results of tensile tests indicate a significant enhancement of the repair bond strength as a result of introducing microfibers to repair layer.

Although various studies indicated the potential effectiveness of fiber reinforcement in improving interface performance, the exact governing mechanisms are neither well understood nor quantified for the different concurring contributing factors, so that accounting for these effects in the design and analysis of a repair application can be challenging. For instance, knowledge gaps comprising the collaborative effect of surface preparation/roughness and fiber reinforcement for different fiber types need to be addressed, and so does the distinction between the impact of fibers on ITZ quality (early-age damage prevention such as drying shrinkage [14]) and the contribution to fracture mechanisms such as crack deviation, kinking, or trapping [11,13,16,18].

The main objective of the work presented hereafter is to provide a contribution towards the understanding of complex mechanisms involved with the interfacial cracking in cement-based bi-material systems. The study is focused on testing and characterization of fracture in Mode-I for different types of fiber reinforced concretes (the repair materials) and, especially, their bond to an older, unreinforced concrete (the substrate). Beyond the plain, unreinforced control condition, volume fractions of 0.5% and 1% with three types of fibers were considered for the repair material, namely: (i) 8 mm long Poly-Vinyl-Alcohol (PVA) fibers, (ii) 12 mm long PVA fibers (to compare the effects of different fiber lengths), and (iii) 13 mm long steel fibers (to compare fibers with similar lengths but different materials, matrix bonding, and stiffness). Both PVA and steel fibers were selected because this reinforcement can be very effective at enhancing the mechanical performance of concrete and especially its fracture toughness, with the potential also for strain hardening behavior in tension. In addition, both PVA and steel fibers can be very good at preventing or mitigating cracking related to volume changes such as shrinkage, a crucial property in repair applications where optimum compatibility between old and new concrete needs to be achieved to prevent damage acceleration. Previous studies have shown that both PVA and steel fibers can enhance concrete-concrete bond [11,14,15,18], although most of the information available is focused on shear bond and very limited information is available on progressive debonding in Mode I. Studies also indicate that steel fibers can be more effective than PVA fibers at lower volume fractions while, conversely, PVA fibers can be more effective at higher volume fractions. Moreover, regarding shear bond, PVA have proven more effective than steel fibers in applications with minimum interfacial roughness (i.e., smooth interface, no sandblasting) [18]. In this study, the Mode-I crack propagation was investigated through a Countered Double Cantilever Beam (CDCB) test [15], supported by imaging techniques for stress-strain analysis. Fracture parameters were computed based on a classic Modified Linear Elastic Fracture Mechanics (MLEFM) approach. No bonding agent was applied but the substrates were sandblasted to enhance interfacial roughness before applying the repairs. Interfacial roughness and crack deviation were quantified through laser scanning; correlations between surface topography and fracture parameters were analyzed.

2. Materials and Methods

2.1. Materials and Specimen Preparation

The mix proportions of substrate and repair materials are shown in Table 1. General use hydraulic cement and class F fly ash were used. Fine aggregate was natural sand and coarse aggregate was crushed rock with a maximum size of 10 mm. For the repair materials, beyond the plain control condition without fibers, three types of fibers with volume fractions $V_f = 0.5\%$ and 1% were considered, namely: (i) 8 mm long Poly-Vinyl-Alcohol (PVA) fibers, (ii) 12 mm long PVA fibers (to compare the effects of different fiber lengths), and (iii) 13 mm long steel fibers (to compare fibers with similar lengths but very different materials, matrix bonding, and stiffness). As reported at the state of the art and discussed in the introduction, short fibers can be more effective than longer fibers with respect to bonding especially because their effectiveness depends upon the relative size of the fiber compared to the interface roughness. The technical information on the fibers is provided in Table 2.

Table 1. Mix proportions of substrate and repair layers.

Layer	Cement	Fly Ash	Sand	10 mm Aggregate	Water	Fiber Volume Fraction
Substrate	1	0.25	2	0.48	0.5	—
Repair	1	0.25	2	—	0.5	0%, 0.5% & 1%

Table 2. Technical information about Poly-Vinyl-Alcohol (PVA) and steel fibers adopted.

Type of Fiber	Diameter [mm]	Cut Length [mm]	Tensile Strength [MPa]	Young's Modulus (GPa)	Specific Gravity
8 mm PVA	0.04	8	1600	40	1.3
12 mm PVA	0.10	12	1100	28	1.3
13 mm Steel	0.20	13	2750	210	7.85

For the composite substrate-repair samples, concrete substrates were cast in pre-formed moulds designed to cast only half of the final specimen. Substrates were covered by plastic sheets immediately after casting, demoulded after 24 h, and eventually placed in cured at a standard temperature of $20\text{ }^{\circ}\text{C} \pm 2\text{ }^{\circ}\text{C}$ and humidity $95\% \pm 5\%$. After 28 day curing, the substrates were sandblasted. Sandblasting was done by a pressure washer at 4000 PSI (27.6 MPa) using a commercially available glass abrasive product containing less than 1% silica. The nozzle was kept at a distance of 10–20 cm from substrate surface for 1–2 minutes up to the point that the aggregate would be visible on the substrate surface. Afterwards, concrete substrates were put back into the moulds in optimum Saturated Surface Dry (SSD) condition [19] and the repair mortar was poured against the substrates. It is important to mention that, in this work and unlike in other studies, the mortar was cast parallel to the substrate. Although the mortar was well vibrated and compacted, this casting direction is expected to potentially penalize compaction at the Interfacial Transition Zone by the substrate and to affect fiber orientation near the bond plane (especially for steel fibers, which are stiffer). The repaired specimens were cured with the same procedure used for the substrates. When casting the substrate and repair components of the specimens for bond testing, monolithic specimens of the repair materials were cast in similar CDCB moulds and cured together with the bond samples, in order to characterize fracture properties of the repair materials as well. Three replicates were tested for each of the seven repair materials and each of the seven corresponding concrete-repair interfaces.

2.2. Experimental Methods and Testing Set-up

Countered Double Cantilever Beam (CDCB) tests were conducted to analyze Mode-I substrate-repair debonding and to assess crack growth resistance of the repair materials. The study was based on a Modified Linear Elastic Fracture Mechanics (MLEFM) approach, comprising the analysis of fracture toughness versus effective crack length response curves. In addition, imaging technique for displacement analysis was employed with the purpose of visualizing crack and strain patterns during the test. Finally, 3D surface scans were conducted to obtain substrate roughness profiles.

2.2.1. Countered Double Cantilever Beam (CDCB) test

In general, tensile bond tests can be subdivided into direct and indirect methods. The main flaw of direct tensile tests is their high sensitivity to the specimen anchoring system and to slight eccentricities, which might lead to bending effects at the interface or premature material failure rather than bond failure [20]. Indirect tensile tests, such as flexural and splitting methods, on the other hand, can help overcome some of these issues, although the indirect nature of the stresses applied may introduce some computational challenges. There is a long tradition of splitting fracture tests to determine the fundamental mechanical behavior of materials and of bi-material systems [13,19]. The technique using a Double Cantilever Beam specimen was first developed for structural adhesives and eventually adapted to studying fracture properties of monolithic materials [21] as well as interfaces in cement-based bi-material systems [15]. The DCB test consists of applying a splitting load to propagate a crack in a pre-notched specimen while recording the applied load and the opening displacement of the crack faces, with the major benefit that several fracture parameters can be investigated. In addition, more reliable compliance measurements are possible (as described in the following sections) as the test geometry promotes the application of smaller splitting loads and larger displacements compared to other test setups [21]. Further studies suggested tapering the samples in order to make the rate of the strain release theoretically independent of the crack length, hence leading to a more stable crack propagation. This specific condition can be achieved by shaping the sample so that the rate of change of the compliance is theoretically constant during the crack growth (as detailed in the following sections). The resulting geometry was re-named the Contoured DCB (CDCB) test (Figure 1), also known as the linear compliance test [21].

Geometrical proportions and size of the specimen tested are shown in Figure 1a,b and follow the set-up introduced by [15]. A side groove along the desired crack plane promotes a proper crack growth and hinders any unfavorable crack deviation in monolithic specimens (Figure 1a). In this study, however, the test was also adapted to the fracture analysis of interfaces, with the specimen subdivided into two symmetrical parts, that is, the concrete substrate on one side, the repair material on the other side, and the bond plane in between, running exactly along the CDCB middle section (Figure 1b). For those bi-material tests, the interface represents a plane of weakness by itself, and to avoid excessive damage during handling, the side groove was removed from the middle line (Figure 1b). This aspect was properly computed in the back-calculations discussed below.

The test was performed using a servo-hydraulic Instron universal testing machine (Figure 1e). Specimens were supported by a hinge fixed to the lower plate of the testing machine, while the upper part were supported by a steel profile with two identical wedges, which were used to apply the splitting load. Each wedge was positioned between two low-friction bearings mounted on both sides of the CDCB sample by means of steel rods passing through the section (and placed above the crack so that this would not be affected, Figure 1d). The steel profile was connected to a load cell, which was connected to the cross head of the machine. Although the specimen was subjected to a vertical load in addition to the horizontal splitting load (SL), this vertical component can be ignored by keeping the angle of the wedge, $\alpha = 15^\circ$ (Figure 1d), small and by employing low friction needle bearings so that the coefficient of friction, μ , between the wedge and bearings can be reasonably neglected [15]. The displacement rate was kept on average at 0.02 mm/min, to promote more stable crack propagation.

During the test, load and Crack Mouth Opening Displacement (CMOD) were recorded continuously. The CMOD (Figure 1c) was measured with a gauge transducer measuring the relative displacement near the base of the notch and was also monitored by means of the 2D Digital Image Correlation (DIC) technique (Figure 2) [22,23]. The values obtained with the sensor and with DIC were consistent. For the data acquisition using DIC, a high-speed 9-megapixel mvBlueFox camera in combination with the GOM SNAP software were adopted; the collected data was processed using the GOM Correlate software. The camera was placed at a distance of 1.7 m from the specimen. Beforehand, a speckle pattern of black dots over a white background was applied on the surface of specimens by means of spray painting. The light was adjusted at every test to guarantee an even illumination of the specimen and to avoid over-exposure. Since the crack propagation test needs to be performed at a slow displacement rate to allow stable crack propagation, the maximum acquisition frequency was set to 0.5 Hz.

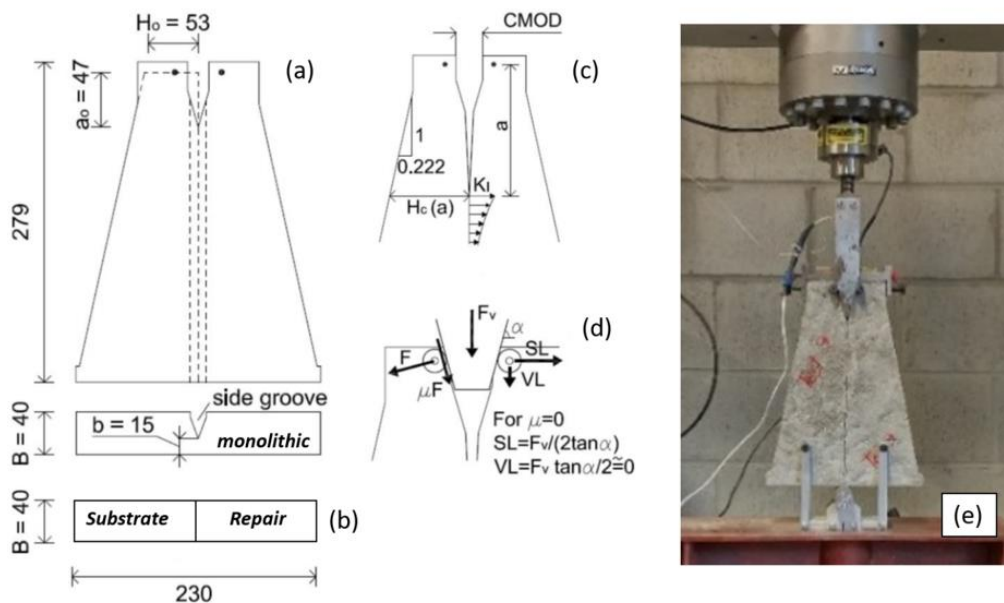


Figure 1. (a) Countered double cantilever beam (CDCB) specimen geometry and (b) adaptation for testing of bi-material systems, (c) parameters for crack growth resistance analysis, (d) calculation of forces applied, and (e) test setup [15].

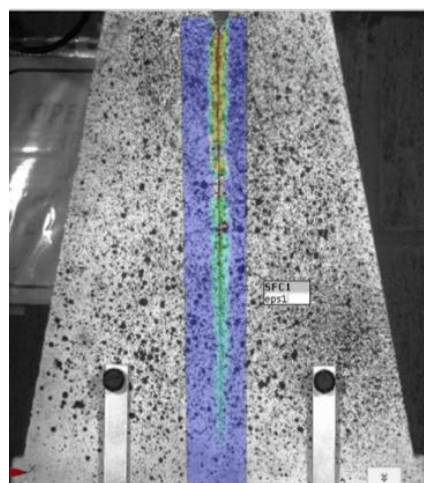


Figure 2. Representative black dot pattern, with location of the region of interest (ROI) around the interface for Digital Image Correlation.

2.2.2. Roughness profiles and quantification of crack deviation

Surface roughness analysis was performed with different purposes, namely: (i) To assess crack tortuosity of monolithic material samples after failure, and (ii) to assess the roughness of the substrates after sandblasting (prior to casting the repair material) in the composite samples for interfacial bond studies.

The topography of the sandblasted substrates was monitored performing 3D laser scanning of the surfaces (Figure 3a) by means of a Nikon – 3D Cross Scanner with the accuracy of 8 μm and inspection/scan software (Focus 10.0). Several parameters have been introduced to quantify surface roughness. In this study, the mean peak height (S_{pm}) and the average roughness (S_a) parameters were selected [24–26]. These parameters have been suggested as reliable roughness parameters [27,28]. S_{pm} was calculated as the average of the maximum peak height (p_i) from each sampling length where sampling length is equal to 1/5 of the total length, while S_a was given by the arithmetic mean of the absolute values $Z(x,y)$ within sampling length (l) and sampling width (b).

$$S_{pm} = \frac{1}{5} \sum_{i=1}^5 p_i \tag{1}$$

$$S_a = \frac{1}{lb} \int_0^l \int_0^b |Z(x,y)| dx dy \tag{2}$$

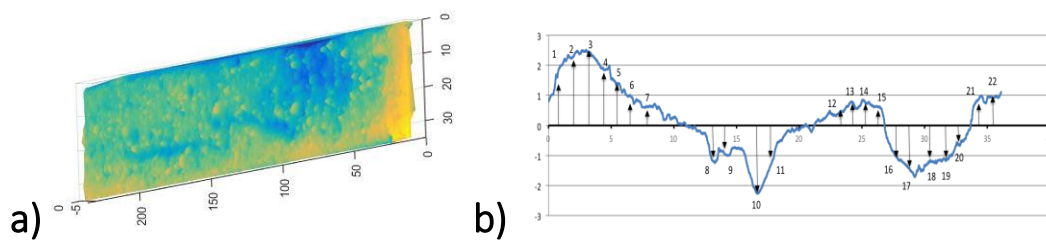


Figure 3. (a) Representative three-dimensional (3D) topography of a substrate profile after sandblasting and prior to the repair application and (b) two-dimensional (2D) profiles used to calculate crack deviation in monolithic, material tests.

In order to quantify crack deviation in the materials tests (monolithic specimens) and to reduce the computational load, the authors deemed sufficient to perform a 2D image analysis of the crack profile. To this end, 2D images of the crack profiles after the failure taken and processed with a commercial image processing software with accuracy of 70 μm to calculate the area below the deviated crack with respect to the mid-line (Figure 3b). This area represents a quantification of crack deviation.

2.2.3. Calculation of Fracture Parameters

Ideally, brittle materials are the ones that can be characterized by the propagation of one single crack with the elastic zones near the crack. For fracture analysis of such materials, the linear elastic fracture mechanics (LEFM) theory can be applied. LEFM indicates that the fracture instability of brittle materials in Mode-I or opening mode can be defined by only one parameter, i.e., the critical stress intensity factor (K_{IC}) or the specific fracture energy (G_f) [15].

Back to Griffith [29], a crack propagates unstably when the rate of change in the elastic energy released by the system for a unit crack extension (U), is equal or higher than the energy required for the crack to propagate within the material, for a unit crack extension (W):

$$G_{IC} = \frac{\partial U}{\partial a} = \frac{\partial W}{\partial a} = R \tag{3}$$

where G_{IC} = Mode-I critical strain energy release (or specific fracture energy G_f), a = crack length and R = crack growth resistance. The stress intensity factor, K_I , that defines the elastic stress field intensity ahead of the crack is then sufficient to characterize the whole stress field around the crack. K_I reaches K_{IC} (critical value) when enough energy is supplied to the system and unstable crack propagation occurs.

The LEFM theory is applicable in materials where the zone around the crack that undergoes inelastic deformations remains small and is therefore neglected. However, in the case of cement-based materials (typically referred to as quasi-brittle materials), a large zone of damaged material, known as fracture process zone (FPZ), subject to high stress concentration, develops around the crack tip. Micro-cracking along the FPZ improves the energy absorption capability because it causes less energy flux released into the crack tip and increased cracking surface area [30]. The extension of FPZ affects toughness of quasi-brittle materials as well as tortuosity and bridging effects of aggregate and unbroken ligaments [31,32].

There are various, well-calibrated classic methods for analysing the behavior of the FPZ, including fracture models proposed by Bažant and Cedolin [33], Hilleborg [34], de Borst [35], Rots [36], Rots and Blaauwendraad [37], Bažant [30], and Reinhardt and Cornellisen [38]. In the analysis of the CDCB test, a methodology was developed [15,21,39] for the computation of crack growth resistance curves based on the effective crack model. With this approach, the effect of the FPZ is accounted for by treating the quasi-brittle material as a brittle material with an increased, fictitious crack length, called effective crack length (a_{eff}). By treating the material as brittle, a Modified Linear Elastic Fracture Mechanics (MLEFM) based on adaptation of LEFM [32] equations can still be utilized. The typical crack-growth-resistance curves of brittle and quasi-brittle materials (or interfaces, in case of bi-material systems) are represented in Figure 4a. In brittle systems, the crack propagates unstably since formation and, hence, its resistance to propagation (here represented by the stress intensity factor) is a straight, horizontal line, unrelated to crack extension. In the case of quasi-brittle systems, the toughening mechanisms occurring after crack nucleation allow for a stage of stable (nonlinear) crack growth, represented by an initial rising trend (BOP-B), followed by a flat branch of unstable propagation after critical crack length and critical stress intensity factor are reached, point B of Figure 4a.

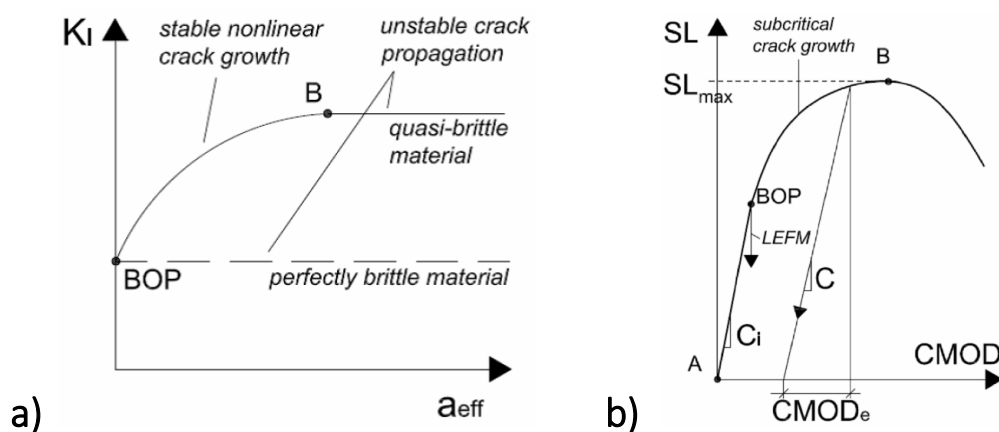


Figure 4. (a) Typical crack-growth-resistance curves of brittle and quasi-brittle materials and (b) typical response of quasi-brittle materials under CDCB test [15].

A typical Splitting Load (SL)-Crack Mouth Opening Displacement (CMOD) response curve obtained from the CDCB test of quasi-brittle materials or bi-material interfaces (for bond tests) is represented in Figure 4b. Three main stages can be identified, namely: (i) Initial linear elastic behavior (A-BOP), (ii) stable, subcritical crack growth (BOP-B) upon crack formation, here identified at the curve Bend Over Point (BOP), and (iii) unstable crack propagation (after the critical crack length is achieved at point B). These stages are related to the aforementioned stages depicted in Figure 4a. In order to

compute the crack growth resistance curves (Figure 4a) from the experimental curves (Figure 4b), a procedure based on experimental and theoretical compliances [40] was employed. The compliance (C) is defined as the ratio between the elastic component of the CMOD (CMOD_e, Figure 4b) and the corresponding splitting load (SL):

$$C = \frac{CMOD_e}{SL} \tag{4}$$

To calculate the experimental compliance based on the experimental CMOD and SL data, it is possible to neglect the permanent deformation during the subcritical crack growth (CMOD_e = CMOD, Figure 4b), by assuming a return to the origin upon unloading.

Considering MLEFM, each specimen arm at one of the crack sides can be considered as a simple cantilever beam made of a perfectly elastic material. With reference to the strength-of-materials approach, the theoretical compliance can be calculated as follows by considering bending and shear deformations of the beam:

$$C_{th} = \frac{2\Delta}{SL} = \frac{CMOD}{SL} = \frac{24}{EB} \int_0^a \frac{x^2}{H^3} dx + \frac{6(1+\nu)}{EB} \int_0^a \frac{1}{H} dx \tag{5}$$

where E = Young’s Modules, Δ = arm displacement, B = beam width (specimen depth), ν = Poisson’s ratio and a = crack length. Since the beam height is variable, a constant equivalent height equal to the mean height is considered:

$$H_c = \frac{H_o + H_a}{2} = H_o + \frac{ma}{2} \tag{6}$$

where H_o is the width of the top of the beam and H_a is the beam height at distance a from the loading point.

Equation 5 was written based on the assumption that the end of the cantilever beam is fixed. However, the actual rotation of the bottom edge around the supporting hinge (Figure 1) needs to be considered. Based on the findings by [41], this can be amended by increasing the beam length by adopting an equivalent, increased crack length equal to a + 0.6H_c. As a result, Equation 5 can be re-written as follows:

$$C_{th}(a) = \frac{24}{EB} \left\{ \frac{[a + 0.6H_c(a)]^3}{3H_c^3(a)} + \frac{0.3a}{H_c(a)} \right\} \tag{7}$$

By equating the initial experimental compliance to the initial theoretical compliance prior to BOP (Figure 4b), the effective modulus of elasticity (E_{eff}) is determined. The initial experimental compliance (C_{exp,i}) is calculated at the BOP, that is the first point of nonlinearity. Considering that the crack length before the BOP is equal to the length of the notch (a₀), the initial theoretical compliance is given by:

$$C_{th,i} = C_{th}(a_0) \tag{8}$$

Once E_{eff} is known, the effective crack length (a_{eff}) is calculated by equating the experimental compliance to the theoretical one at each point of the SL-CMOD curve. Hence, the Mode-I SIF (K_I) for a CDCB sample is determined from :

$$K_I^2 = \eta^2 SL^2 B^{-2} H_a^{-3} (a^2 + 1.4aH_a + 0.5H_a^2) \tag{9}$$

where η is a function of the slope and here is equal to 3.1 for m = 0.222 41.

Considering that one B parameter in B⁻² stands for beam depth and one for crack depth, when crack depth and beam depth are not equal to each other (in the case of monolithic specimens, Figure 1a) one of the B parameters has to be changed to b (crack depth, Figure 1a). Hence, Equation 9 is re-written as follows for monolithic specimens with side-groove:

$$K_I^2 = \eta^2 SL^2 (Bb)^{-1} H_a^{-3} (a^2 + 1.4aH_a + 0.5H_a^2) \tag{10}$$

Based on this approach, crack growth resistance curves of repair materials and substrate-repair interface bond were computed using the software MATLAB.

3. Results and Discussion

3.1. Mode-I crack growth resistance of the repair materials

As anticipated, plain mortar specimens exhibited a brittle, abrupt failure soon after initial crack nucleation, while more controlled, steady crack propagation was observed in the fiber reinforced mortars overall at both pre-peak crack nucleation and post-peak crack propagation. Failure occurred along the groove at the mid section as desired.

Experimental Splitting Load (SL) compared to crack mouth opening displacement (CMOD) curves obtained with 8 mm PVA fibers are shown in Figure 5a, where the curve of the plain repair material is also plotted for comparison. Only one type of fiber is shown here for the sake of conciseness, but all the different SL-CMOD curves obtained are available in the Appendix A. The allowable maximum crack width for durability of FRC structures ranges from 150 to 300 μm , with the most stringent requirements specified by the American Concrete Institute (ACI) 224R [42]. According to ACI 224R the maximum crack width at the tensile face of reinforced concrete structures is specified as 150 μm for exposure conditions of seawater, seawater spray, wetting, and drying, and 180 μm for deicing chemical exposure. The FRCs investigated here achieve those crack opening values within the stable stage of subcritical crack growth prior to achieving the peak of the response curve and the unstable crack propagation in most cases, or otherwise exhibit significant residual stresses (Figure 5a, Figure A1a–c).

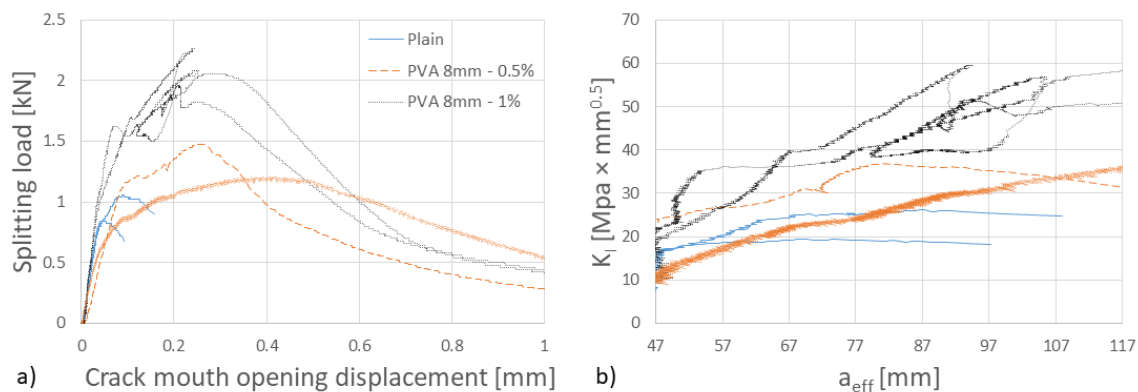


Figure 5. (a) Splitting load (SL) versus crack mouth opening displacement (CMOD) curves of 8 mm PVA fiber reinforced concrete (FRC) and (b) crack growth resistance curves (in terms of SIFs, K_I , compared to effective crack length, a_{eff}) of 8 mm PVA FRC.

Average values of the peak splitting loads of the different repair materials (representing the onset of unstable crack propagation, point B of Figure 4) are plotted as a function of the fiber type and content (V_f) in Figure 6a. As expected, a consistent increase of the peak SL is observed for increasing fiber contents, with steel fibers reaching the highest values. With $V_f = 1\%$ of the steel fiber, SL is increased from 0.8 kN to 2.8 kN (around 250%). The same contents of 8 mm and 12 mm long PVA fibers provide 175% and 87.5% SL increments, respectively. With a lower V_f , the SL increment is 75%, 62.5%, and 50% with steel, 8 mm PVA, and 12 mm PVA fibers. Therefore, the incremental benefit from 0.5% to 1% V_f is much higher than the one from 0% to 0.5% V_f .

Crack growth resistance curves in terms of stress intensity factor (K_I) and effective crack length (a_{eff}) were calculated following the procedure described in 2.2.3. Additionally in this case, only one representative fiber type is shown in Figure 5b and compared to the plain repair mortar, while the full curves for the other fiber types are available in the Appendix A. Compared to the plain repair material, fiber reinforced concretes exhibited a considerably greater subcritical crack growth branch (BOP-B, Figure 4) before the onset of the unstable propagation. The critical stress intensity factors (K_{IC}), which

represent the initiation of unstable crack propagation, are plotted in Figure 6b for different fiber types and contents. Consistently with the trends observed for the peak SL, K_{IC} increased for increasing fiber contents and the highest increment were obtained with 1% V_f steel fibers.

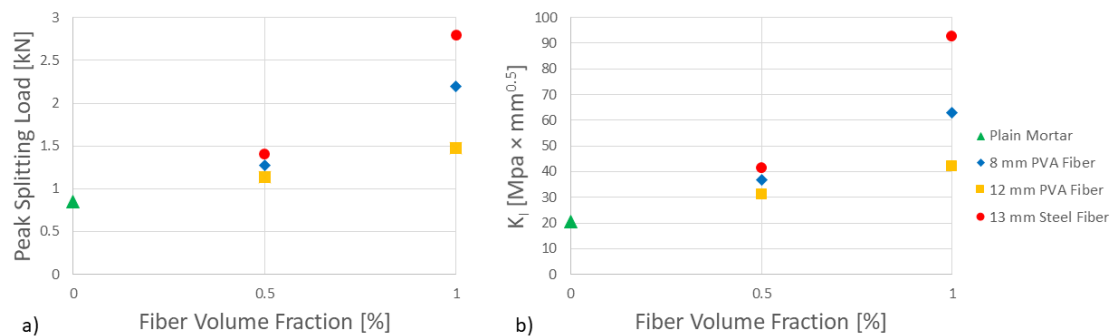


Figure 6. (a) Peak splitting loads (SL) and (b) critical stress intensity factors (K_I) obtained for various fiber types and volume fractions.

Microcracks encounter a higher toughness and crack growth resistance in the presence of fibers. Some fibers develop a chemical bond with the cementitious matrix that causes stress redistribution around the crack tip, promotes crack blunting, and bridges the cracks. This favors the tortuosity of the crack and causes directional deviations. It is expected that larger crack deviation leads to greater crack growth resistance.

Quantitative correlations between crack deviation quantified as shown in Figure 3b (Section 2.2.2) and the peak splitting load are investigated (Figure 7a). It can be observed that higher values of the splitting load correspond to the greater crack deviation. This is due to the fact that fibers are able to blunt cracks and deviate them. In this way, more energy is dissipated and higher values of the splitting load can be obtained. As crack deviation increases, the enhancement of the splitting load becomes more significant. Figure 7b shows dissipated energy (G) versus crack deviation. G corresponds to the area under the SL-CMOD curve beyond the peak splitting load up to the crack width of 1 mm. While Figure 7a represents the ability of fibers in mitigating subcritical crack growth, Figure 7b demonstrates the effectiveness of fibers in controlling unstable crack propagation beyond the peak splitting load. For instance, plain mortar shows slight subcritical crack growth resistance, however, it cannot hinder unstable crack propagation beyond the peak splitting load. By comparing Figure 7a with Figure 7b, one can also observe at which stage of the crack propagation each solution is more effective. For instance, increasing the 8 mm PVA fiber content from 0.5% up to 1% affects the subcritical crack growth (peak SL, Figure 7a), but the post-peak behavior remains unchanged as similar G values are obtained for the two V_f values (0.5% and 1%).

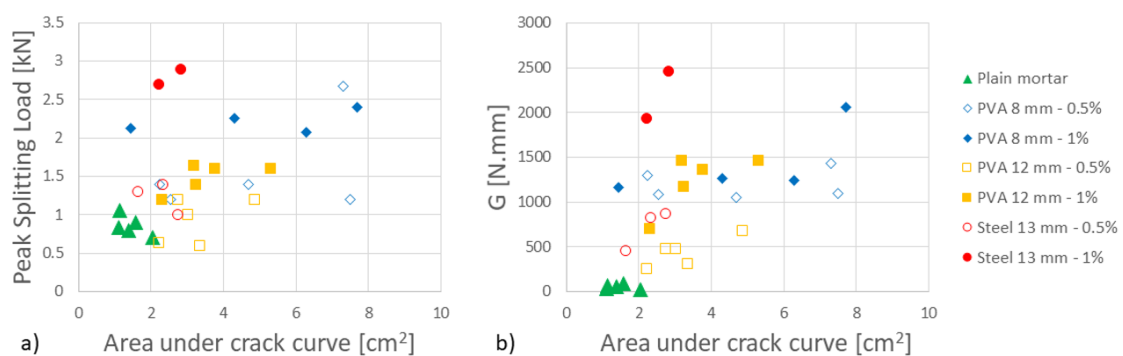


Figure 7. (a) Peak splitting load and (b) post-peak fracture energy versus crack deviation with respect to the midline.

3.2. Mode-I crack growth resistance of the substrate-repair interfaces (bi-material systems)

The bi-material specimens failed at the interface as expected, with the failure plane passing through and nearby the bond plane. Given the interfacial tortuosity achieved through the substrate roughness treatment (sandblasting), some slight deviation of the failure plane from the bond plane was expected and, in fact, desired, as this is a known toughening mechanism in interfacial cracking [12,15]. Same as for the material result discussion, the experimental response curves (SL-CMOD) obtained for only one representative type of fibers (8 mm PVA) are shown in Figure 8a, while the bond response curves obtained with other fibers are available in the Appendix A. Crack growth resistance curves obtained using the MLEFM approach described in Section 2.2.3 are shown in Figure 8b for 8 mm PVA fibers and in the Appendix A for the other fiber types. Similar to the FRC materials discussed above, though for smaller values of Splitting Load and Crack Mouth Opening Displacement, concrete substrate-FRC repair interfaces still exhibited a stable, subcritical crack growth (Figure 8).

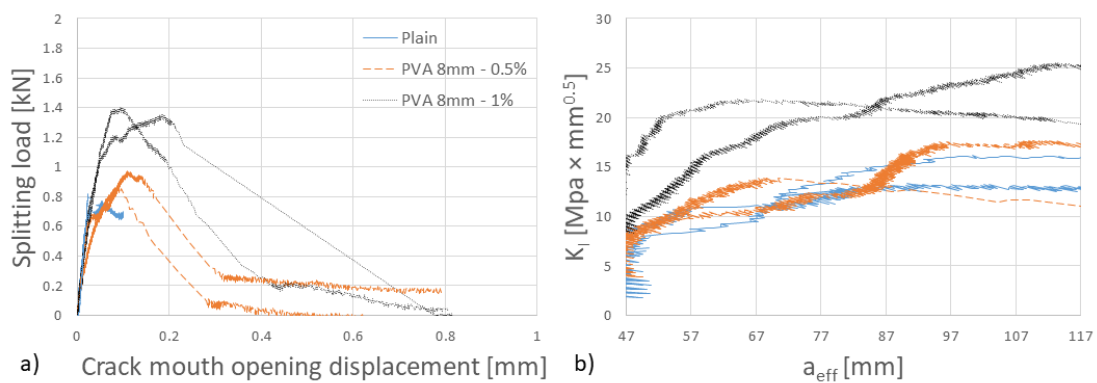


Figure 8. (a) Splitting load (SL) versus crack mouth opening displacement (CMOD) curves of concrete-FRC interfaces and (b) crack growth resistance curves in terms of stress intensity factor, K_I , versus effective crack length, a_{eff} .

Crack propagation after the peak SL, however was quite different. Two main types of post-peak crack propagation were identified, namely: (i) Quick failure along the interface followed by sample split up in two parts along the concrete – concrete interfaces (Figure 9a), and (ii) micro-crack deviations from the interface followed by slower failure and slight residual splitting load (Figure 9b).

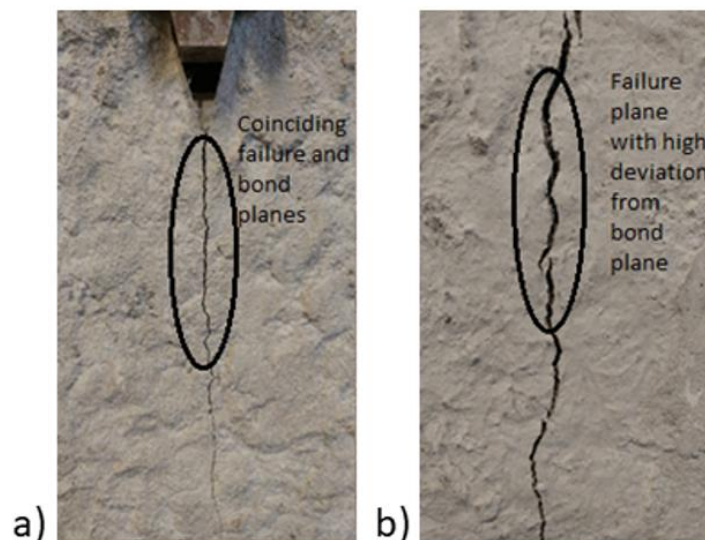


Figure 9. Representative failures of the interface for (a) lower crack deviation and (b) higher crack deviation.

Figure 10a. reports average Mode-I strength values and corresponding fiber volume fractions for three different types of fiber reinforcement. Mode-I bond strength of repair mortars reinforced with 8 mm long PVA fibers ranges between 1.1 and 1.5 kN. It ranges between 0.8 and 1.1 kN for 12 mm long PVA fibers and from 1.2 to 1.4 kN for steel fibers. Although most of the samples exhibited a bond failure, in some specimens, partial material and bond failure was observed.

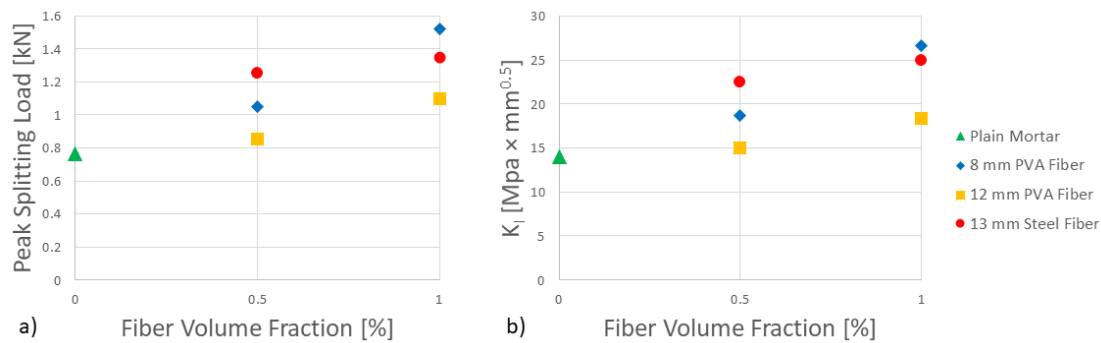


Figure 10. (a) Peak splitting load (SL) and (b) critical stress intensity factor (K_I) of substrate-repair interfaces for various fiber types and volume fractions.

3.3. Substrate-Repair Interface Cracking: Comparison and Discussion

Peak values of the bond splitting load and the critical stress intensity factor, corresponding to the stress intensity factor at the crack tip prior to the start of unstable cracking, are plotted in Figure 10 as a function of fiber type and content. A steady improvement was observed as the fiber content (V_f) was increased. With $V_f = 1\%$, the peak splitting load and critical stress intensity factor are twice as high as those of the plain concrete. However, while steel fibers outperformed PVA fibers in the material fracture tests (Figure 6, Section 3.1), quantitative differences between steel and 8 mm PVA fibers are negligible when it comes to concrete-FRC interfaces (Figure 10). This obviously has to do with the different mechanisms involved with the failure of the material and the failure of the interface.

In the case of concrete-FRC bond, the beneficial effects of fibers can be classified into two main categories as follows:

1. Fibers reduce interfacial damage, help compatibility, reduce shrinkage and bleeding [8,10,16];
2. Fibers can provide additional toughening mechanisms by the interface. This is highly dependent on the mode of fracture, fiber bonding, size relative to the interface roughness, stiffness, and orientation with respect to the bond plane, and overall deviation of the failure plane from the bond plane [11,12,18].

With respect to point 2, it may be useful to investigate how many fibers were intersected by the failure plane during crack propagation. An optical microscope was used for the measurement of the number of fibers along the interface. This information is correlated to the peak Splitting Load in Figure 11 for the different fibers considered. One can observe that there is a consistent trend between the number of PVA fibers that remained attached to the substrate and were crossed by the failure plane (mixed adhesive-cohesive interfacial failure). No significant correlation was found for the number of steel fibers. This has to do with the different fiber sizes, stiffness, and bonding. Nevertheless, steel fibers had a favorable contribution to bond, comparable or superior to that of PVA fibers, thus confirming that, for different fibers, different mechanisms are involved. For PVA fibers, instead (due to their smaller size and different bonding), the number of fibers crossed at failure can be interpreted as an indication of the amount of cohesive rather than purely adhesive splitting occurring by the interfacial area.

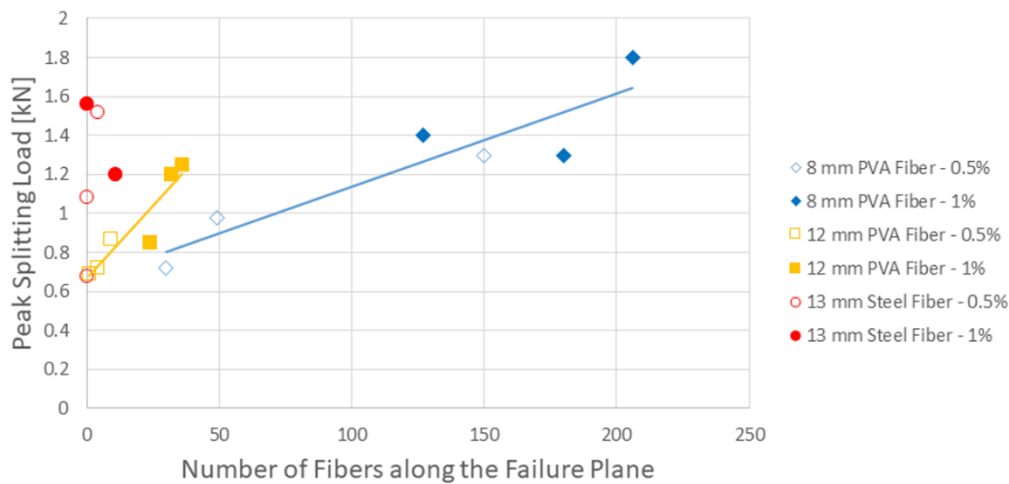


Figure 11. Peak splitting load versus number of fibers along the failure plane after substrate-repair splitting.

In light of the good correlation found in Figure 11 for PVA fibers, the analysis was extended to investigating possible correlations between the number of fibers crossed by the failure plane and the roughness of the interface. Although the sandblasting was performed in the same manner for all the specimens, differences in the roughness parameters obtained (especially when calculated on a relatively small interface area) are inevitable. Based on the 3D surface scanning procedure and analysis described in Section 2.2.2, roughness quantification parameters were obtained. To the best of the authors’ knowledge, there is no other work at the state of the art that investigates the correlation between quantitative roughness parameters and concrete-concrete bond parameters under Mode-I fracture tests. In this work, the authors investigated the correlation between quantitative roughness parameters and Mode-I crack growth resistance parameters. It was found that the average roughness (S_a) exhibited the best correlation with the splitting load (Figure 12a). However, this finding cannot be generalized and other bond strength/cracking parameters (e.g., in Mode-II) may be best correlated to other roughness parameters. Interestingly, the peak SL- S_a trends are not as clear as the ones depicted in Figure 11 for peak SL versus number of PVA fibers attached to the failure plane. While the peak SL was best correlated to S_a , the number of PVA fibers crossed by the failure plane was found to be best correlated to S_{pm} , a parameter that depicts the maximum topographical gaps in the roughness profile (Figure 12b).

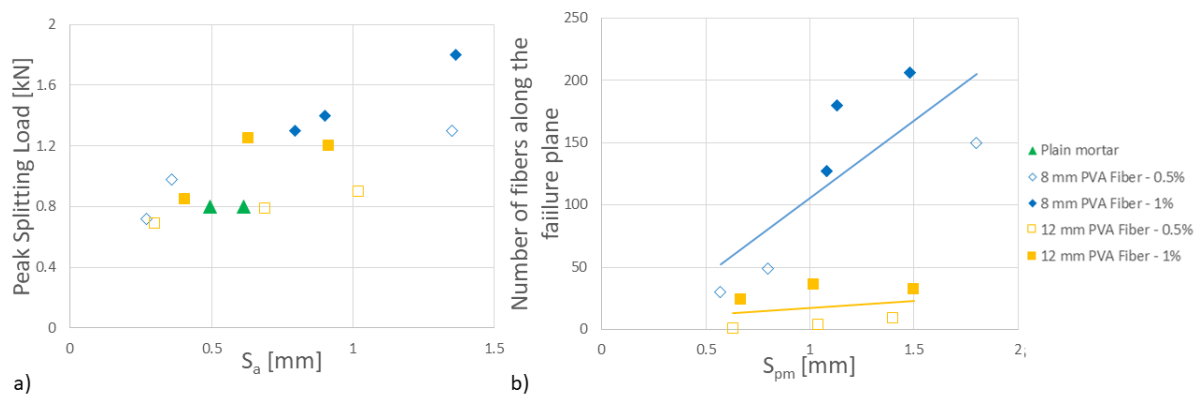


Figure 12. (a) Peak splitting load versus S_a and (b) number of PVA fibers along the failure plane after testing vs. S_{pm} .

4. Concluding Remarks

An experimental program was presented to study the effects of different fiber reinforcements on substrate-repair debonding in Mode-I. Volume fractions of 0%, 0.5%, and 1% of 8 mm long PVA fibers, 12 mm long PVA fibers, and 13 mm long steel fibers were evaluated. The role of different fibers in improving interfacial bond and crack growth resistance was investigated. The role of crack deviation on the Mode-I strength of monolithic specimens was investigated. Moreover, the impact of interfacial roughness was studied. Using 3D surface scans and optical microscope, the relationship between repair material/fibers intersected at failure and the Mode-I bond strength was investigated. The main conclusions can be summarized as follows:

1. Significant enhancement of the Mode-I crack growth resistance was observed in the repair materials and in the substrate-repair bond after introducing fiber reinforcement in the repair.
2. In the repair materials, a significant enhancement of the overall crack growth resistance curves, peak Splitting Load (SL) and critical stress intensity factors were observed for increasing fiber contents, as anticipated. For instance, peak SL increments of 50%–75% and 87%–250% were achieved at 0.5% and 1% V_f , respectively, with steel fibers providing the highest increases. Consistent correlations were found between the Mode-I crack growth resistance of the repair materials and quantified crack deviation, confirming the ability of fibers to promote crack tortuosity as one of their different contributing mechanisms to crack growth resistance.
3. For the concrete-concrete interfaces, 8 mm PVA fibers were the fibers exhibiting the best performance at $V_f = 1\%$, while, in case of $V_f = 0.5\%$, 13 mm steel fibers reached the highest fracture values. This has to do with a number of contributing factors, including the stiffness and size of the fibers with respect to the roughness of the interface (as far as failure mechanisms are concerned), the bonding of the fiber to the matrix, as well as the effect of fibers on compaction near and at the Interfacial Transition Zone, the different ability of different fiber types and contents to mitigate or prevent shrinkage/thermal cracking and bleeding.
4. Substrate roughness and interfacial tortuosity had a significant impact on Mode-I crack growth resistance. Minor changes in quantified substrate roughness parameters affected fracture parameters (such as the peak splitting load) and, for PVA fibers, also affected the amount of fibers intersected by the failure plane during splitting.
5. For PVA fibers, a correlation was also found between the fracture parameters and number of fibers intersected by the failure plane. This was not the case for steel fibers, due to their different stiffness and diameter. Regardless, the beneficial effect of steel fibers on concrete-concrete interfacial crack growth in Mode-I confirms that other bond enhancing mechanisms are in place.
6. The aim of this study was to provide a better understanding of complex mechanisms involved with the interfacial cracking in concrete-concrete composite systems. This information can be used to help the design of repairs and retrofits with fiber reinforced concrete with the scope to optimize stress transfer and durability along the substrate-repair bond, a parameter that is essential to the effectiveness and durability of the retrofitted structure. Finally, the investigation of the mechanisms set a database of information for the modeling of concrete-FRC debonding in Mode-I.

Author Contributions: Two authors contribute equal to the paper.

Funding: This study was funded by the Natural Science and Engineering Research Council of Canada, NSERC (grant number RGPIN-2016-03863).

Conflicts of Interest: The authors declare no conflict of interest.

Appendix A

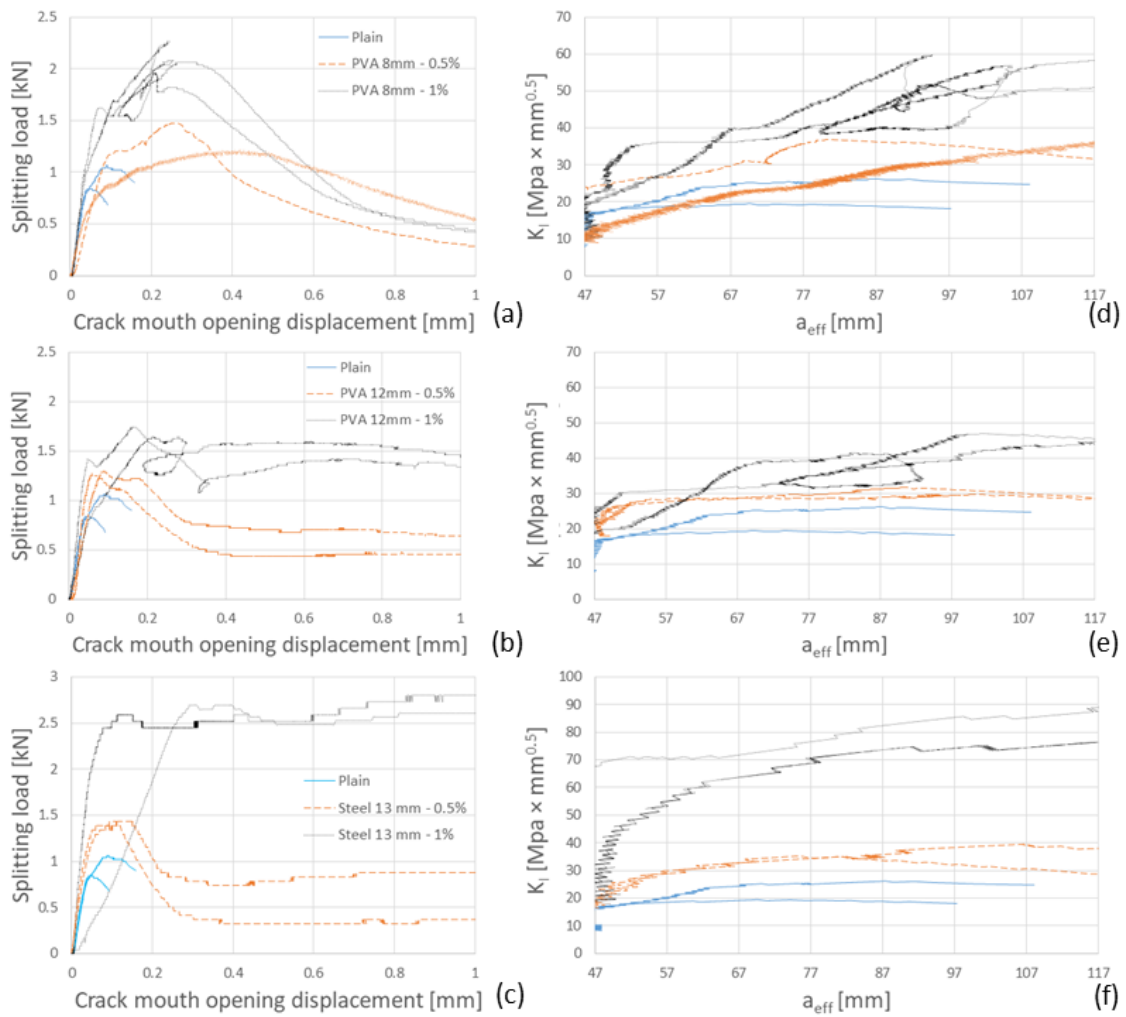


Figure A1. Splitting load (SL) versus crack mouth opening displacement (CMOD) curves of (a) 8 mm PVA FRC; (b) 12 mm PVA FRC; (c) 13 mm Steel FRC, crack growth resistance curves (in terms of SIFs, K_I) versus effective crack length, a_{eff} of (d) 8 mm PVA FRC; (e) 12 mm PVA FRC; (f) 13 mm steel FRC.

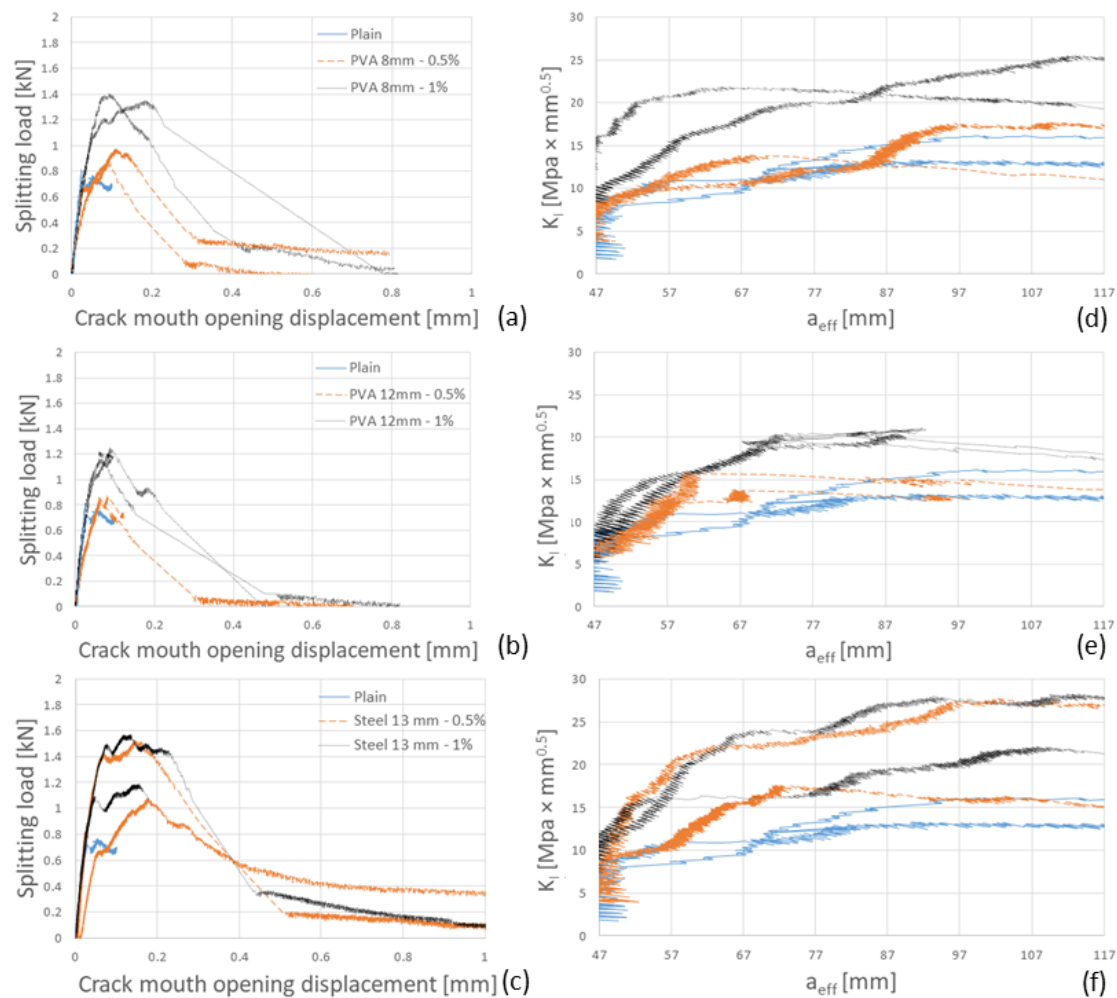


Figure A2. Splitting load (SL) versus crack mouth opening displacement (CMOD) curves of (a) 8 mm PVA interface; (b) 12 mm PVA interface; (c) 13 mm Steel interface, crack growth resistance curves (in terms of SIFs, K_I versus effective crack length, a_{eff}) of (d) 8 mm PVA interface; (e) 12 mm PVA interface; (f) 13 mm steel interface.

References

1. Sadowski, L.; Stefaniuk, D.; Hola, J. The effect of the porosity within the interfacial zone between layers on pull-off adhesion. *Constr. Build. Mater.* **2017**, *152*, 887–897. [[CrossRef](#)]
2. Sadowski, L. Multi-Scale Evaluation on the interphase Zone between the Overlay and Concrete Substrate: Methods and Descriptions. *Appl. Sci.* **2017**, *7*, 893. [[CrossRef](#)]
3. Courard, L.; Piotrowski, T.; Garbac, A. Near-to-surface properties affecting bond strength in concrete repair. *Cem. Concr. Compos.* **2014**, *46*, 73–80. [[CrossRef](#)]
4. Xiong, G.; Liu, J.; Li, G.; Xie, H. A way for improving interfacial transition zone between concrete substrate and repair materials. *Cem. Concr. Res.* **2002**, *32*, 1877–1881. [[CrossRef](#)]
5. Sadowski, L.; Stefaniuk, D. Microstructural Evolution within the Interphase between Hardening Overlay and Existing Concrete Substrates. *Appl. Sci.* **2017**, *7*, 123. [[CrossRef](#)]
6. Qi, C.; Wiess, J.; Olek, J. Characterization of plastic shrinkage cracking in fiber reinforced concrete using image analysis and a modified Weibull function. *Mater. Struct.* **2003**, *36*, 386–395. [[CrossRef](#)]
7. Bentur, A.; Mindess, S. *Fiber Reinforced Cementitious Composites*; Taylor and Francis: New York, NY, USA, 2007.
8. Banthia, N.; Zanotti, C.; Sappakittipakorn, M. Sustainable fiber reinforced concrete for repair applications. *Constr. Build. Mater.* **2014**, *67*, 405–412. [[CrossRef](#)]
9. Barkhordari Bafghi, M.A.; Amini, F.; Safaye Nikoo, H.; Sarkardeh, H. Effect of Steel Fiber and Different Environments on Flexural Behavior of Reinforced Concrete Beams. *Appl. Sci.* **2017**, *7*, 1011. [[CrossRef](#)]

10. Banthia, N.; Gupta, R. Influence of Polypropylene Fiber Geometry on Plastic Shrinkage Cracking in Concrete. *Cem. Concr. Res.* **2006**, *36*, 1263–1267. [[CrossRef](#)]
11. Lim, Y.M.; Li, V.C. Durable repair of aged infrastructure using trapping mechanism of engineered cementitious composites. *Cem. Concr. Compos.* **1997**, *19*, 373–385. [[CrossRef](#)]
12. Li, V.C. On engineered cementitious composites: A review of the material and its applications. *J. Adv. Concr. Technol.* **2003**, *1*, 215–230. [[CrossRef](#)]
13. Wagner, C.; Bretschneider, N.; Slowik, V. *Characterization of the Interface between Strain Hardening Cementitious Repair Layers and Concrete subgrade*; FraMCoS-8: Toledo, Spain, 2013.
14. Slowik, V.; Lukovic, M.; Wagner, C.; Van Zijl, G. Behaviour of bonded SHCC overlay systems. In *A Framework for Durability Design with Strain-Hardening Cement-Based Composites (SHCC)*; Chapter 8; Van Zijl, G.P.A.G., Slowik, V., Eds.; RILEM, Springer: Netherlands, 2017; pp. 125–146. ISBN 978-94-024-1012-9.
15. Zanotti, C.; Banthia, N.; Plizzari, G. Towards sustainable repairs: Substrate-repair interface Mode-I fracture analysis. *Intl. J. Sust. Mater. Struct. Syst.* **2014**, *1*, 265–281. [[CrossRef](#)]
16. Zanotti, C.; Banthia, N.; Plizzari, G. A study of some factors affecting bond in cementitious fiber reinforced repairs. *Cem. Concr. Res.* **2014**, *63*, 117–126. [[CrossRef](#)]
17. Banthia, N.; Moncef, A.; Chokri, K.; Sheng, J. Micro-fiber reinforced cement composites. *Uniaxial Tensile Response Can. J. Civ. Eng.* **1994**, *21*, 999–1011. [[CrossRef](#)]
18. Zanotti, C.; Rostagno, G.; Tingley, B. Further evidence of interfacial adhesive bond strength enhancement thorough fiber reinforcement in repairs. *Constr. Build. Mater.* **2018**, *160*, 775–785. [[CrossRef](#)]
19. Momayez, A.; Ehsani, M.R.; Ramezani-pour, A.A.; Rajaie, H. Comparison of methods for evaluating bond strength between concrete substrate and repair materials. *Cem. Concr. Res.* **2005**, *35*, 748–757. [[CrossRef](#)]
20. Austin, S.; Robins, P.; Youguang, P. Tensile bond testing of concrete repairs. *Mater. Struct.* **1995**, *28*, 249–259. [[CrossRef](#)]
21. Genois, I. Fracture Resistance of Micro-Fiber Reinforced Cement Composites. Ph.D. Thesis, University of British Columbia, Department of Civil Engineering, Vancouver, BC, Canada, 1995.
22. Tekieli, M.; De Santis, S.; De Felice, G.; Kwiecien, A.; Roscini, F. Application of Digital Image Correlation of Composite Reinforcement Testing. *Compos. Struct.* **2017**, *160*, 670–688. [[CrossRef](#)]
23. Dai, S.; Liu, X.; Nawnit, K. Experimental Study on the Fracture Process Zone Characteristics in Concrete Utilizing DIC and AE Methods. *Appl. Sci.* **2019**, *9*, 1346. [[CrossRef](#)]
24. ISO 4287-1997. *Geometrical Product Specification—Surface Texture: Profile Method—Terms Definitions and Surface Texture Parameters*; International Organisation for Standardisation: Geneva, Switzerland, 1997.
25. EN, B. 1-1:2004. Eurocode 2: Design of Concrete Structures. In *General Rules and Rules for Buildings*; European Committee for Standardization: Brussels, Belgium, 2004; 225p.
26. CAN/CSA A23.3. *Design of Concrete Structures—Structures Design*; Canadian Standards Association: Rexdale, ON, Canada, 2004; 258p.
27. Santos, P.M.D.; Júlio, E. Interface shear transfer on composite concrete members. *ACI Struct. J.* **2014**, *111*, 133–121.
28. Mohamad, M.E.; Ibrahim, I.S. Interface shear strength of concrete-to-concrete bond with and without projecting steel reinforcement. *J. Teknol.* **2015**, *75*, 169–172. [[CrossRef](#)]
29. Griffith, A.A. The phenomena of rupture and flow in solids. *Philos. Trans R. Soc. Lond. Ser. A* **1920**, *221*, 163–198. [[CrossRef](#)]
30. Bazant, Z.P. Fracture mechanics of concrete structures. In Proceedings of the First International Conference (FraMCoS-1), Breckenridge, CO, USA, 1–5 June 1992; Elsevier: London, UK, 1040p.
31. Mindess, S. The fracture process zone in concrete. In *Toughening Mechanisms in Quasi Brittle Materials*; Shah, S.P., Ed.; Kluwer Academic Publishers: Dordrecht, The Netherlands, 1991; pp. 271–286.
32. Van Mier, J.G.M. Mode I fracture of concrete: Discontinuous crack growth and crack interface grain bridging. *Cem. Concr. Res.* **1991**, *21*, 1–15. [[CrossRef](#)]
33. Bazant, N.; Cedolin, L. Blunt crack bond propagation in finite element analysis. *J. Eng. Mech. Div.* **1979**, *105*, 297–315.
34. Hilleborg, A. Analysis of fracture by means of the fictitious crack model, particularly for fiber reinforced concrete. *Int. J. Cem. Compos.* **1980**, *2*, 177–184.

35. De Borst, R. Application of advanced solution techniques to concrete cracking and non-associated plasticity. In *Numerical Method for Non-Linear Problems*; Taylor, C., Hinton, E., Owen, D.R.J., Onate, E., Eds.; Pineridge Press: Swansea, UK, 1984; Volume 2, pp. 314–325.
36. Rots, J.G. Computational Modelling Of Concrete Fracture. Ph.D. Thesis, Civil Engineering and Geosciences, Delft University of Technology, Delft, The Netherlands, 1988.
37. Rots, J.C.; Blaauwendrad, J. Crack models for concrete: Discrete or smeared? Fixed, multi-directional or rotating. *HEORN* **1989**, *34*, 1–59.
38. Reinhardt, H.; Cornelissen, H.A.W. Post-peak cyclic behaviour of concrete in uniaxial tensile and alternating tensile and compressive loading. *Cem. Concr. Res.* **1994**, *14*, 263–270. [[CrossRef](#)]
39. Sorelli, L.; Banthia, N.; Plizzari, G.A. Crack growth resistance of thin mortar layers with hybrid fiber reinforcement. American Concrete Institute: Farmington Hills, MI, USA. *Spec. Publ.* **2014**, *224*, 161–178.
40. Visalvanich, K.; Naaman, A.E. Fracture methods in cement composites. *J. Eng. Mech. Div.* **1981**, *107*, 1155–1171.
41. Mostovoy, S.; Crosley, P.B.; Ripling, E.J. Use of crack-line-loaded specimens for measuring plane strain fracture toughness. *J. Mater.* **1967**, *2*, 661–681.
42. ACI 224R-01. *Control of Cracking in Concrete Structures*; ACI Committee 224; American Concrete Institute: Farmington Hills, MI, USA, 2001.



© 2019 by the authors. Licensee MDPI, Basel, Switzerland. This article is an open access article distributed under the terms and conditions of the Creative Commons Attribution (CC BY) license (<http://creativecommons.org/licenses/by/4.0/>).